RSC Advances

PAPER

View Article Online
View Journal | View Issue

Cite this: *RSC Adv.*, 2021, **11**, 34392

Gel-based precursors for the high-performance of n-channel GaInSnZnO and p-channel CuGaSnSO thin-film transistors†

Ravindra Naik Bukke and Jin Jang*

Received 21st June 2021
Accepted 5th October 2021

DOI: 10.1039/d1ra04787f

rsc.li/rsc-advances

The performance of metal–oxide thin-film transistors (TFTs) should be further improved for the applications of next-generation displays. Here, the developments of gel-derived gallium–indium–tin–zinc oxide (GITZO) for n-channel and copper–gallium–tin–sulfide oxide (CGTSO) for p-channel TFTs are demonstrated. The a-GITZO film by gel-based precursor gives an excellent interface with ZrO_x compared to the GITZO deposited using pristine or purified precursor. The gel-derived GITZO TFT exhibits the saturation mobility (μ_{sat}) of 28.6 ± 2.15 $cm^2\ V^{-1}\ s^{-1}$, three-fold higher than the pristine one, and excellent bias stability. The boost in GITZO TFT performances is due to the purity of the metal oxide material and higher film density with smooth surface morphology. In addition, the field-effect mobility (μ_{FE}) of the p-channel copper–tin–sulfide–gallium oxide (CGTSO) TFT could be increased from 1.71 to 4.25 $cm^2\ V^{-1}\ s^{-1}$ using a gel-derived precursor solution. Therefore, these results demonstrate that the gel-derived metal–oxide precursor by the solution process is a promising one for the high performance of the TFT backplane.

Introduction

Thin-film transistors (TFTs) based on transparent metal–oxide (M–O) are of increasing interest to replace Si-based TFTs.[1,2] Binary oxides, such as ZnO, In_2O_3, and SnO_2, are popular compounds for oxide semiconductors. Their structures are mostly polycrystalline, and thus have grain boundary (GB) between crystalline grains. To improve the TFT performance, multi-component oxide semiconductors are of increasing interest, such as zirconium–indium–zinc oxide (ZIZO), aluminum–zinc–tin oxide (AZTO), amorphous indium–gallium–zinc oxide (a-IGZO), amorphous indium–zinc–tin oxide (a-IZTO), amorphous aluminum–indium–zinc–tin oxide (a-AIZTO), amorphous gallium–indium–zinc–tin oxide (a-GIZTO), yttrium–indium–zinc–tin oxide (YIZTO), lithium–indium–zinc–tin oxide (LIZTO), and magnesium–indium–zinc–tin oxide (MIZTO).[2–16] The most attractive application of MO TFTs is active-matrix backplanes for organic light-emitting diode (OLED) display due to their high mobility, high transparency in the visible region, and low-cost production with solution process.[17,18] A vacuum process, such as sputtering, plasma-enhanced chemical vapor deposition, and atomic layer deposition, needs high manufacturing cost for display application.[19,20] Therefore, solution processes, such as spray coating, ink-jet printing, and spin coating, are widely studied.[21–30] The high mobility TFT backplanes are required for the large area, high-resolution, and high frame-rate display. A high mobility amorphous M–O TFT over >10 $cm^2\ V^{-1}\ s^{-1}$ can be achieved by the solution process,[31–33] but its stability is a critical issue to be solved. To enhance the electrical performance of solution-processed MO TFTs, a typically higher annealing temperature (typically >400 °C) is required.[34,35] It should be noted that there is no degradation in the device performance based on the polyimide (PI) substrate due to its higher endurance temperature over 450 °C.[34,35] Crystalline semiconductor films induce oxygen-related defects (*i.e.*, oxygen vacancies and hydroxyl groups) at the interface between the gate insulator (GI) and channel layers, giving an inferior performance, including high leakage currents in TFT.[19,35,36]

Impurities in the precursor solutions yield films with poor quality. The preparation methods of MO precursor solution with high purity were reported to address this issue, such as "sol–gel on-chip",[36] thermally purified solution (TPS),[37] metal–oxide precursor solution purification,[6,26] and the chemical energetic combustion process using fuel and an oxidizer.[27,28,38] The combustion, purification and TPS process could lead to chemical reactions together with pre-hydrolysis by thermal energy in the MO-based precursor solution. These chemical reactions can improve the MO film quality.[6,22,26–28,38] Likewise, the chemical additives (such as solvents, stabilizers, and dopants) and simple precursor modification routes (for example, TPS, gels) are used to obtain better semiconducting

Advanced Display Research Center, Department of Information Display, Kyung Hee University, Hoegi-dong, Dongdaemun-gu, Seoul 130-701, South Korea. E-mail: jjang@khu.ac.kr

† Electronic supplementary information (ESI) available. See DOI: 10.1039/d1ra04787f

materials, which provides a good quality (*i.e.*, continuous, as well as crack-free) thin film at low temperatures.[26,36–39]

The structural disorder increase by a chemically derived multi-component MO material could lead to a stable amorphous semiconductor oxide film.[40–44] In a previous report, Ga-doped IZTO TFT (350 °C) using AlO_x as a gate insulator exhibits the mobility of 11.80 $cm^2 V^{-1} s^{-1}$ ($V_{DS} = 0.1$ V, and $V_{GS} = 3$ V).[10] H. Yang *et al.* reported that Ga-doped ITZO TFT (350 °C) exhibits mobility higher than 30 $cm^2 V^{-1} s^{-1}$ ($V_{DS} = 40$ V, and $V_{GS} = 20$ V). Nomura *et al.* reported the percolation conduction mechanism in multicomponent MO with heavy transition metal cations with $(n-1)d^{10}ns^0$ ($n \geq 5$) electronic configuration.[1] For high mobility, the selection of metal cations with large ionic radii and spherically symmetric 4s, 5s, and/or 6s electron orbitals can increase the degree of wavefunction overlap as electron delocalization, and finally enhance electron mobility even in an amorphous state. The metal cations, such as In^{3+} and Sn^{4+}, have a similar electronic configuration of $4d^{10}5s^0$ as the path for carrier transport in the amorphous MOS, which is the key feature to ensure high mobility,[4] although the achievability of increased mobility and nearly stable IGZTO TFTs has been reported.[11–15] It should be noted that the M–O bond enthalpy and Lewis acid strength ($L = z/r^2$, where z and r were ionic radius and atomic charge number, respectively) play a critical role in improving the device stability.[49] Nevertheless, the main reason for using multi-components in the oxide system is to achieve a stable M–O network and to realize the high performance of amorphous metal oxide TFTs.[45–49]

To develop oxide-based complementary metal–oxide–semiconductor (CMOS) circuits, high field-effect mobility (μ_{FE}) of p-type semiconductors is necessary. In a p-type MO semiconductor, the carrier conduction path is formed by anisotropic, localized O 2p orbitals in the valence band, leading to a large hole effective mass and low hole mobility (μ_h). In the binary metal–oxide, SnO TFT exhibits a higher μ_{FE} over 1 $cm^2 V^{-1} s^{-1}$ compared to NiO and CuO TFTs due to the delocalized Sn 5s states at the valence band (VB).[50–52] The pseudo-metal halides, such as copper-thiocyanate (CuSCN) with a bandgap (~3.5 eV), exhibits lower mobility of ~0.1 $cm^2 V^{-1} s^{-1}$, which is relatively low even when operating at a high voltage (>10 V).[53] Copper–tin–sulfide–gallium oxide (CTSGO) is one of the emerging materials for p-type MO semiconductors owing to its favorable bandgap.[54,55] Therefore, developing p-type MO semiconductors has become of utmost importance for high-performance, low-power TFT electronics.

This study reports the effect of gel-based precursors on the performance of solution-processed n-type a-GITZO and p-type CTSGO TFTs. The gel-derived GITZO TFT exhibits the saturation mobility (μ_{sat}) of 28.6 ± 2.15 $cm^2 V^{-1} s^{-1}$, three-fold higher than the pristine one, subthreshold swing (SS) of 133 mV dec^{-1}, and an ON/OFF current ratio (I_{ON}/I_{OFF}) of 5.1×10^8. The GITZO TFT has zero hysteresis voltage and a small ΔV_{TH} shift of 0.15 V upon PBTS at $V_{GS} = 5$ V for 1 h in the dark. The flexible GITZO TFT on the polyimide (PI) substrate exhibits a field-effect mobility of 11.89 $cm^2 V^{-1} s^{-1}$ and zero hysteresis voltage. On the other hand, the μ_{FE} of the p-channel CTSGO TFT increases from 1.71 to 4.25 $cm^2 V^{-1} s^{-1}$ by using a gel-derived precursor solution. These enhancements of the TFT performances are due to the higher film density, smooth surface roughness, and fewer oxygen-related defects in the film, which are confirmed from X-ray reflectivity (XRR), atomic force microscopy (AFM), and X-ray photoelectron spectroscopy (XPS), respectively. Therefore, the gel-derived metal–oxide precursor is a promising approach to improve both n- and p-channel TFTs for next-generation display applications.

Experimental section

Precursor solution synthesis

Gallium nitrate hexahydrate ($Ga(NO_3)_3 \cdot H_2O$) (25.57 mg), indium chloride ($InCl_3$) (884.72 mg), tin chloride ($SnCl_2$) (758.48 mg), and zinc chloride ($ZnCl_2$) (545.20 mg) precursors were mixed into a 20 mL of 2-methoxyethanol (2ME) to prepare the GITZO precursor solution. The solution was stirred under N_2 environment for at least 2 h to obtain a transparent and homogenous solution at room temperature. A 0.1 M CTSGO precursor solution was prepared by adding copper(II) acetate monohydrate ($CuC_4H_6O_4 \cdot H_2O$), thiourea (NH_2CSNH_4), tin chloride ($SnCl_2$), and gallium(III) nitrate hydrate ($Ga(NO_3)_3 \cdot H_2O$) into 2ME, and the solution was stirred for 5 h. All precursor materials were purchased from Sigma Aldrich. The purification of the precursor solution was performed by using a Büchi rotary evaporator. The pristine GITZO or CTSGO precursor solution was poured into a 250 mL round bottom flask connected with a vacuum chamber. The water bath temperature increased from room temperature to 95 °C in 30 min with a step of 10 °C, where the evaporation of the solvent starts at ~70 °C. Finally, the GITZO/CTSGO gel-derived precursor could be obtained at 95 °C, was kept at the same temperature for ten minutes, and then cooled down to RT. The synthesis for the extraction of the gel-derived precursor and the respective photographs for pristine, gel-derived, and purified GITZO precursor solutions are shown in Fig. 1a. Both the pristine and gel-derived GITZO precursors are dissolved in 2ME, whereas a mixture of ethylene glycol and acetonitrile (EG + AC) was used for the purified solution. All precursor solutions were transparent and filtered using a 0.45 μm polytetrafluoroethylene (PTFE) filter.

Thin-film and TFT fabrication

The fabrication process flow for the GIZTO thin film is shown in Fig. S1a (ESI†). We fabricated a-GITZO TFTs using the staggered bottom-gate structure (bottom gate and top contact) shown in Fig S1b (ESI†). First, a 40 *n*m molybdenum (Mo) film was sputtered at 280 °C on a glass substrate and patterned as a gate electrode. A ZrO_x layer was deposited on the Mo-patterned substrate by spin-coating (at 3500 rpm for 30 s) and curing at 200 °C on a hot plate for 5 min. This process was repeated twice to achieve the desired thickness of ~35 nm. Finally, the ZrO_x film was annealed at 300 °C for 2 h in an air furnace.[23] Then, the pristine or purified gel-based GITZO layer was deposited by spin coating (at 4000 rpm for 30 s) and curing at 140 °C on a hot plate for 5 min. The GITZO layer was patterned for active islands. The devices were annealed at various temperatures from 250 to 350 °C. Finally, a 40 nm Mo layer was sputtered and patterned

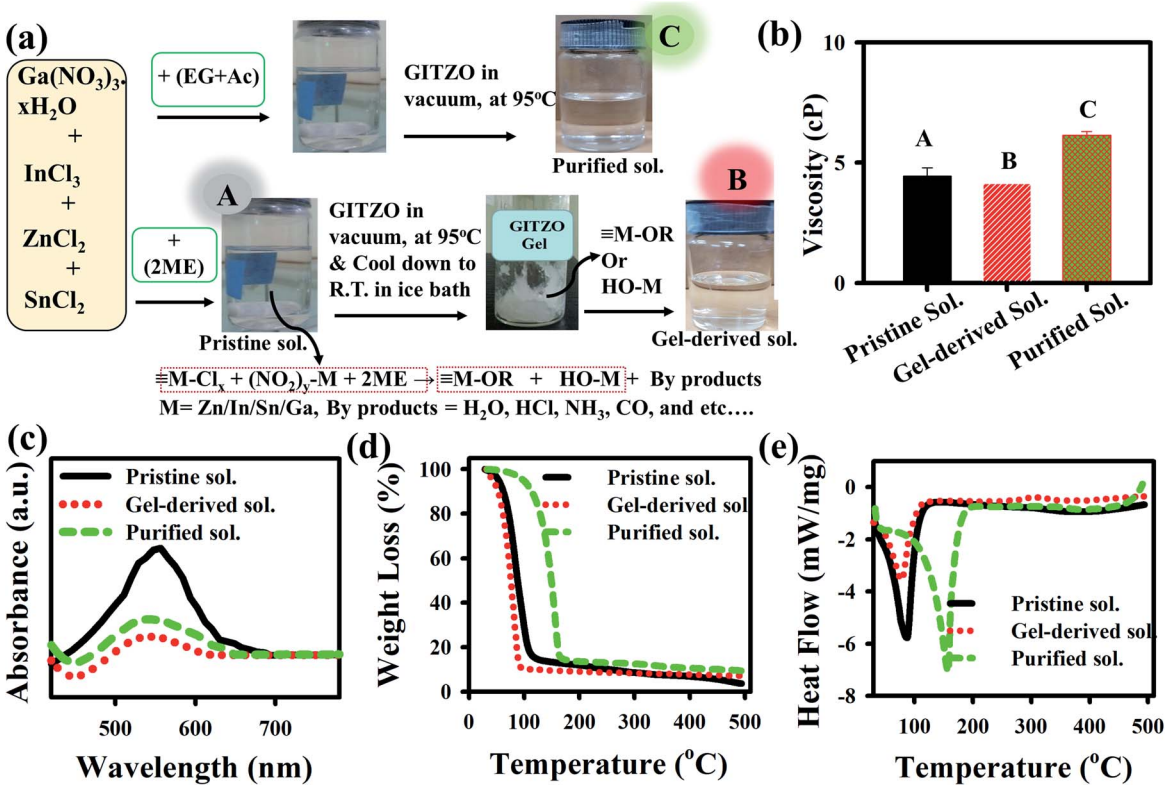

Fig. 1 Synthesis and chemical analysis of the GITZO precursor solution. (a) Extraction of the gel-GITZO precursor product from pristine GITZO precursor solution using a rotary evaporator. The whole system was kept under vacuum, and the water bath temperature increased from RT to 95 °C. The comparison for the (b) viscosity, (c) absorption for the pristine, gel-derived, and purified solution-derived GITZO precursor solution. (d and e) Thermogravimetric analysis (TGA) and differential thermal analysis (DTA) for the weight loss and heat flow as a function of temperature. The GITZO precursor solution at a heating rate of 10 °C min^{-1} in an ambient condition. The gel-derived GITZO precursor dissolved in 2-methoxyethanol (2ME) solvent, and the solvent for the purified solution is a mixture of ethylene glycol and acetonitrile (EG + AC).

for the source and drain (S/D) electrodes. For flexible GITZO TFT, the polyimide (PI) substrate was used. The detailed fabrication process flow of the PI substrate can be found elsewhere.[45]

Material and thin-film characterization

We characterized the GITZO precursor solution by thermo gravimetric-differential thermal analysis (TG–DTA) for thermal decomposition, ultraviolet-visible (UV-vis) spectra for transmittance (UV-visible spectroscopy, Scinco S-4100), and ^{1}H Nuclear Magnetic Resonance (^{1}H NMR) spectra for impurity analysis. The viscosity of the precursor solution was measured by Brookfield DV-III+ Rheometer. The optical bandgap can be obtained using the formulae, $(\alpha h\nu)^2 = A(h\nu - E_g)$, where $h\nu$, α, A, and E_g are the photon energy, absorption coefficient, a proportionality constant, and optical bandgap, respectively. The mass density was extracted by X-ray reflectivity (XRR) analysis. We analyzed the structural and morphological properties of the GITZO thin film by measuring the X-ray diffraction (XRD) for crystal structure and atomic force microscopy (AFM) for RMS roughness. An X-ray photoelectron spectroscopy (XPS) measurement was conducted to examine the chemical composition and elemental analysis in the MO films using the PHI 5000 Versa Probe (PHI 5000 Versa Probe, Ulvac-PHI) at a basic pressure of 7.5×10^{-5} mTorr.

Evaluation of the TFT characteristics

The electrical properties of TFTs were measured by an Agilent 4156C semiconductor parameter analyzer. The transfer characteristics were measured at the drain voltage (V_{DS}) of 0.1 V by sweeping the gate voltage (V_{GS}) from −3 to +3 V. The output characteristics were measured at the drain voltage (V_{GS}) from 0 to 3 V with a step of 1 V by sweeping the gate voltage (V_{DS}) from 0 to +3 V. The field-effect mobility in the saturation region ($V_{DS} \geq V_{GS}-V_{TH}$) was obtained by using eqn (1); the threshold voltage (V_{TH}) was determined from the x-axis intercept of the $(I_{DS})^{1/2}$ *vs.* V_{GS} plot by linear extrapolation method. The saturation mobility was calculated from the linear part of the $(I_{DS})^{1/2}$ *vs.* V_{GS} curve. The linear mobility (μ_{lin}) was measured by using eqn (2); the subthreshold swing (SS) was obtained from the linear region of the log(I_{DS}) *versus* V_{GS} fit by using eqn (3);

$$I_{DS} = (W/2L)\mu_{sat}C_{ox}(V_{GS} - V_{TH})^2 \quad (1)$$

$$\mu_{lin} = g_m/((C_{ox}V_{DS})(W/L)) \quad (2)$$

$$SS = d(V_{GS})/d(\log(I_{DS})) \quad (3)$$

where I_{DS}, W/L, μ_{sat}, C_{ox}, V_{GS}, and V_{TH} are the drain current, channel width/length, saturation mobility, capacitance of the

gate oxide, gate voltage, and threshold voltage, respectively. SS stands for the subthreshold swing. g_m is the transconductance and V_{DS} drain to source voltage.

Results and discussion

The influence of viscosity plays a crucial role in achieving a high-quality thin film. The viscosity of pristine, gel-derived, and purified a-GITZO precursor solutions are 4.35, 4.05, and 6.15 cP, respectively, as shown in Fig. 1b. For the precursor solution preparation, 2ME (boiling point, 119 °C; polarity index, 5.5), EG (boiling point, 197 °C; polarity index, 5.4), and AC (boiling point, 71 °C; polarity index, 5.8) were used as solvents. For the purified GITZO precursor solution, a mixture of EG + AC used as a solvent, the viscosity of the pristine GITZO precursor solution is 5.07 cP. After purification, AC is removed, leading to higher viscosity.[6,26] The higher viscosity of the purified GITZO precursor solution is due to the higher viscosity and lower polarity index of the EG solvent. The high-quality thin-film could be achieved by 2ME due to its higher volatility (less than 120 °C) than the EG + AC and EG, enhancing the dehydroxylation process. Fig. 1c shows the comparison of the absorbance spectra for the three GIZTO precursor solutions. The same volumes of each GITZO precursor solution were used to perform the UV-visible absorption spectra to compare the overall composition and the impurity concentration. The absorption spectra of the precursor solutions were measured in the wavelength range of 200 to 1000 nm. The broad absorbance peak appeared in the wavelength range of 370–630 nm (3.35–1.97 eV), indicating the significate reduction of impurities from the GITZO precursor by gel-derived solution compared to the pristine one.[6,56] Therefore, the impurities in MO could be reduced by using a gel-derived precursor.

Thermal decomposition of the precursor solutions was analyzed by thermogravimetric analysis (TGA)/differential thermal analysis (DTA) and Fourier transform infrared spectroscopy (FTIR), respectively. Fig. 1d and e shows the TGA–DTA curves of the GITZO precursor solution. There are two regions in Fig. 1d, 40–120 °C (Region-I) and 120–500 °C (Region-II). The first endothermic reaction with massive weight loss was observed in Region-I. The endothermic peak for pristine and gel-derived precursor solution was obtained at 89.50 and 81.30 °C, respectively, and is correlated with the solvent evaporation/dehydration reaction. It is caused by solvent evaporation and dehydration of the GITZO precursor solution. The slight difference in the shape of the endothermic peaks and weight loss curves could be attributed to the presence of an impurity. The metal precursors solution was decomposed to metal hydroxyl groups (M–OH), and intermediate gaseous fragments, such as H_2O, ammonia (NH_3), and carbon dioxide (CO_2), could be liberated through hydrolysis and pyrolysis. At ~100 °C, the sol–gel film almost converts to metal–hydroxide (M–OH). Then, around 200 °C, the M–OH starts to form a metal–oxygen–metal (M–O–M) network *via* a condensation reaction.[43,44] There is no significant weight loss in Region-II due to the GITZO compound formation that could be completed at <250 °C. Most of the solvent and unwanted organic compounds are removed at <250 °C (since the 2ME boiling point is ~120 °C and ethylene glycol is 180 °C) (Fig. 1d). There is no noticeable heat-flow variation, and weight loss was observed beyond 350 °C. The FTIR spectra of the three GITZO precursor solutions are shown in Fig. S1c (ESI†). The broad peak in the range 470–650 cm^{-1} indicates M–O bonds, and the peaks around 800 cm^{-1} correspond to the –O–M–O– bonds. The peak around 1060 cm^{-1} was assigned as the asymmetric stretching modes of –C–O–C– and C–C bond vibrations in the solvent. The broad peak in 420 cm^{-1} is due to symmetric stretching COO^- vibration, and another broad peak in the range 2850–3500 cm^{-1} indicates an O–H stretching vibration from hydrolysis of the precursor solution. The O–H vibration of the solvent decreases in the gel-derived GITZO precursor solution compared to the pristine one. These results are consistent with TGA–DTA data, where M–OH converts into M–O at ≤250 °C and takes place continuously. ^{1}H Nuclear Magnetic Resonance (^{1}H NMR) spectra for the pristine gel-derived GITZO precursor solution (since 2ME was used as solvent) were quantitatively analyzed. ^{1}H peaks at 4.148 ppm and 4.210 ppm are related to the hydroxyl (–OH) group of 2ME for both pristine and gel-derived GITZO precursor solutions, respectively, and are shown in Fig. S1d (see ESI†). ^{1}H peaks are related to the –OH shift from lower ppm (upward field) to higher ppm (downward field) level, revealing that the gel-derived GITZO precursor solution has smaller –OH groups. It is found that the intensity of the peak (around ~4.2 ppm) is significantly reduced, and the ^{1}H NMR spectra became broad by gel-derived precursor solution, which indicates that the weak –OH bond can break easily.[26,29] Therefore, the gel-derived GITZO precursor solution shows the peak shift, indicating that the electronic environments around the hydrogens of 2ME are modified, which leads to the high quality of the semiconducting oxide film.[26,29]

Contact angle (CA) measurement was performed to analyze the surface of three GITZO films, as shown in Fig. 2a, indicating 48.23, 39.78, and 45.69°, as shown in Fig. S2a (ESI†). The gel-derived GITZO film exhibits a smaller contact angle ($\theta^\circ \approx 39.78^\circ$) compared to the pristine one ($\theta^\circ \approx 48.23^\circ$). The surface energy ($\gamma_s$) could be estimated from the CA from the equation ($\gamma_s = (\gamma_w/4) \times (1 + \cos\theta^\circ)2$), where θ° is the contact angle at equilibrium and γ_w is the water surface free energy. The values of γ_w for the pristine, gel-derived, and purified GITZO precursor-based films are 48.49, 55.94, and 50.84 mJ m^{-2}, respectively (see Fig. S2b, ESI†). The surface energy (γ_s) values of the GITZO films are 33.65, 43.78, and 36.66° mJ m^{-2}. The work adhesion (W_a) values for the GITZO films are 121.29, 128.74, and 123.64° mJ m^{-2} as shown in Fig. S2f (ESI†). Higher γ_s and W_a indicate better adhesion between the semiconductor and the S/D contacts for TFTs. The optical band gap of the pristine and gel-derived GITZO thin films and their corresponding values are 3.45 and 3.53 eV, respectively, as shown in Fig. S3a (ESI†). The optical transmittance spectra of the gel-derived GITZO thin film on the glass substrate are shown in Fig. S3b (ESI†). The gel-derived GITZO thin film exhibits a transmittance of higher than 90% in the visible range. The photograph of a-GIZTO/glass on the ADRC logo can be seen in the inset of Fig. S3b (ESI†). The thicknesses of the pristine GITZO films annealed at 250, 300,

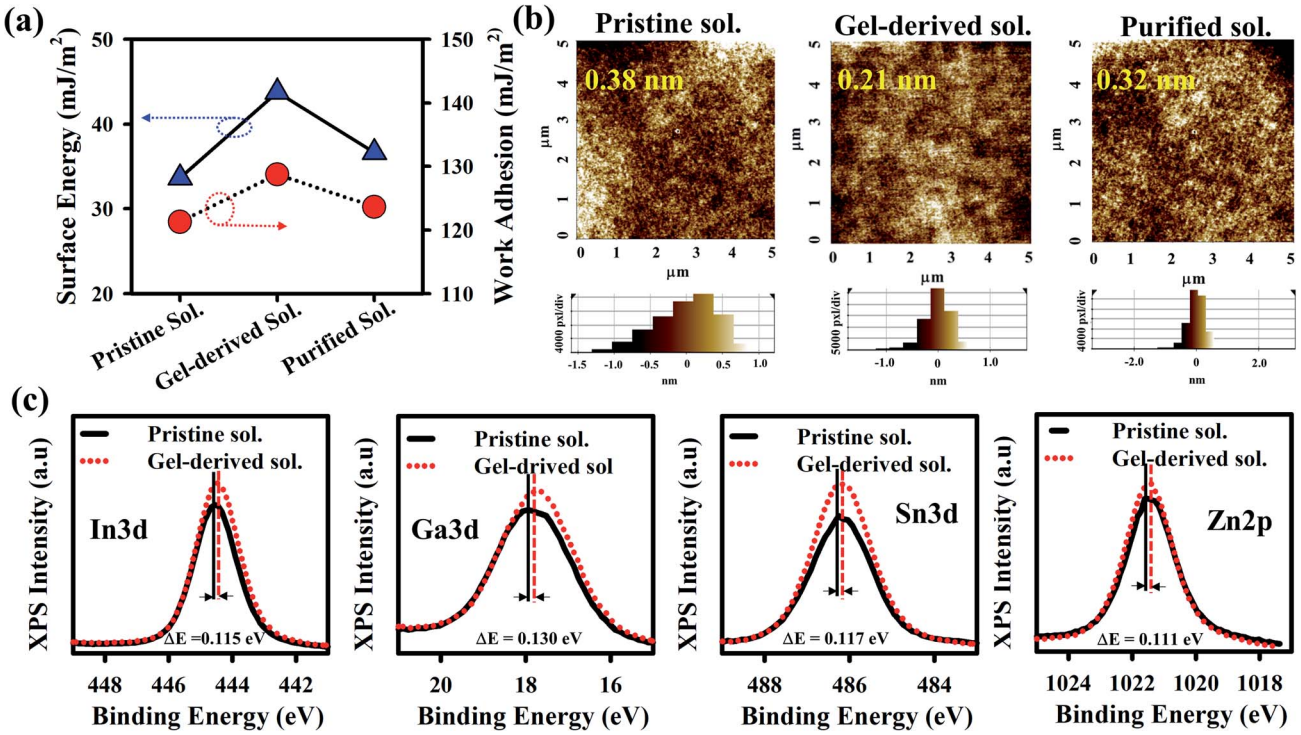

Fig. 2 Surface morphology and chemical bonding analysis of the GITZO films. (a) Surface energy and work adhesion for the pristine, gel-derived, and purified GIZTO films. (b) AFM image (scan size: 5 μm × 5 μm) of three GITZO thin films. The RMS roughness of the GITZO film is lower for the gel-derived precursor material. The smooth surface of the film by gel-derived precursor provides more electron-conducting pathways and reduces the trap density. (c) XPS core-level spectra of In $3d^5$, Ga 3d, Zn $2p^3$, and Sn $3d^5$, obtained from the GIZTO thin films. Their respective peak intensities increase in the gel-derived film. All cation binding energy peaks shift to the lower binding energy, indicating the reduction of oxygen-related defects for the gel-derived GIZTO.

and 350 °C are 11.24, 10.88, and 10.09 nm, and 10.75, 10.13, and 9.52 nm for the gel-derived GIZTO films, respectively. Thicknesses of the optimum GITZO and ZrO_x films were measured using an Alpha-step analyzer, and their corresponding values are 10.13 nm and ~35.0 nm, respectively. The refractive index (RI) values of the pristine, gel-derived, and purified solution based on a-GITZO are 1.77, 1.83, and 1.80, respectively (see Fig. S3c and d, ESI†). RI of the gel-derived a-GITZO films annealed at 250, 300, and 350 °C is shown in Fig S3d (ESI†), and their corresponding RI values are 1.79, 183, and 1.88, respectively. The RI of the MO thin-film can be correlated to the composition of the film density.[21,37,44] The pristine GITZO film has less density, which is related to the defects (such as hydroxyl groups (–OH) and oxygen-related defects) in the film (even after annealing) being significantly reduced by gel-derived GITZO. The increase of the RI value implies the decrease of porosity in the film (since RI ∝ dense film or 1/porosity), which affects the optical and electrical properties of the a-GITZO films. The increase of the film density is confirmed from the refractive index values in the visible range.[21,37,44] Therefore, the dense film with less porosity can be possible by gel-derived GITZO.

The X-ray diffraction (XRD) spectra of three GITZO films are shown in Fig. S4a (ESI†). XRD spectra for the gel-derived GITZO films annealed at 250, 300, and 350 °C are shown in Fig. S4b.† There are no crystalline peaks in GITZO, indicating the amorphous nature. The multi-component metal–oxide film typically exhibits the property of an amorphous structure when the annealing temperature is below 400 °C.[10,21,43] Fig. 2b shows the surface morphology of the three GITZO films. The root mean square roughness (R_{RMS}) values for the pristine, gel-derived, and purified solution-based GITZO films were 0.38, 0.21, and 0.32 nm, respectively. The surface morphology of the pristine and gel-derived GITZO films annealed at various temperatures (*i.e.*, 250 and 350 °C) are shown in Fig. S4c (ESI†). The RRMS values of the pristine GITZO films annealed at 250, 300, and 350 °C, are 0.44, 0.38, and 0.27 nm, respectively, whereas 0.28, 0.21, and 0.18 nm were the R_{RMS} values for the gel-derived a-GITZO precursor. The decrease of the R_{RMS} roughness is attributed to the formation of a uniform, crack-free, and smooth-surface thin film.[5,21,40,43] X-ray photoelectron spectroscopy (XPS) survey scan spectra of the pristine and gel-derived GITZO are shown in Fig. S5a (ESI†), and reveals the presence of oxygen (O), gallium (Ga), zinc (Zn), indium (In), and tin (Sn). The percentages of O : Ga : Zn : In : Sn are 54.13 : 1.03 : 13.16 : 13.69 : 12.94 for pristine GITZO and 51.51 : 1.34 : 15.31 : 15.43 : 14.21 for the gel-derived GITZO film, respectively, as shown in Fig. S5b.† Fig. 2c shows that the XPS spectra of Ga 3d, Zn 2p, In 5s, and Sn 5s binding energy peaks for pristine GITZO are centered at 17.91, 1021.52, 486.29, and 444.56 eV, respectively, whereas it is 17.73, 1021.36, 488.11, and 444.44 eV for the gel-derived GITZO. It is clear that the binding energy peak shifts towards lower energy, which means

more M–O–M network formation. The O 1s spectra of pristine and gel-derived GITZO films are shown in Fig. S5c (ESI†), where the orange color arrow indicates the O 1s peak from the surface to depth. The O 1s peaks shift to higher binding energy in bulk, showing the increase of the M–O–M network.

The electrical properties of a-GITZO TFTs are shown in Fig. 3. Fig. 3a shows the transfer curve and linear mobility as a function of gate voltage for the three a-GITZO TFTs, and the corresponding μ_{sat} (8.02, 24.38, and 13.05) $cm^2\ V^{-1}\ s^{-1}$, V_{ON} of (0.87, 0.91, and 0.36) V, and SS (134, 118, and 103) mV dec^{-1}, respectively. The mobility of gel-derived a-GITZO is higher. It is clear that the based GITZO has higher In and Sn percentage, so that the fraction ([In] + [Sn])/([Ga] + [Zn] + [In] + [Sn] + [O]) increases from 26.10 to 29.53%, as shown in Fig. S5 (ESI†). The identical electron configuration of $4d^{10}5s^0$ and the similar ion radii of the In^{3+} and Sn^{4+} cation provide an effective percolation pathway at the conduction band (CB) edge, which is the key feature to confirm high mobility. The higher fraction of [In] + [Sn] is responsible for increasing the mobility and ON current for gel-based GITZO TFT. The decrease in the SS of a-GITZO TFT suggests the reduction in the interfacial trap density.[7,12] Fig. 3b shows the statistical analysis for the mobility of the pristine, gel-derived, and purified precursor solution-based GIZTO TFTs. The electrical properties of both pristine and gel-derived a-GITZO TFT with various annealing temperature are summarized in Table S1 (ESI†). The transfer and output curves of GITZO TFTs using pristine EG + AC and only EG-solvent-based precursor solutions are shown in Fig. S6a and b (ESI†). It should be noted that both pristine EG + AC and EG solvent-based GITZO TFTs showed inferior electrical properties compared to the purified GITZO precursor solution (see Fig. S6a and b†). The comparison of the transfer curves with hysteresis voltage for the pristine and gel-derived GIZTO TFTs at different annealing temperatures (from 250 to 350 °C) is shown in Fig. S7a–c (ESI†). Fig. S7a–c† shows the leakage current for the GITZO TFT annealed at 250, 300, and 350 °C, respectively. There is no significant change in the leakage currents when the annealing temperature of the active layer varies from 250 to 350 °C. The hysteresis voltage is defined at the I_{DS} of 10^{-10} A with a forward sweep from −3 to +3 V and a reverse sweep from +3 to −3 V. The zero V_H is due to the negligible traps at the gel-derived a-GITZO/ZrO_x interface.[10,22–28,57,58] The presence of electron traps (*i.e.*, hydroxyl groups) at the interface is responsible for the clockwise hysteresis. The statistical analysis for the mobility of gel-derived precursor solution-based GIZTO TFTs at different (250, 300, and 350 °C) annealing temperatures are summarized in Fig. 3c, where 25 TFTs in each case were measured. Mobility of the gel-derived GIZTO TFT increases from 10.10 ± 2.12 to 28.60 ± 2.15 $cm^2\ V^{-1}\ s^{-1}$ by varying the annealing temperature from 250 to 350 °C. It should be noted that the gel-derived a-GIZTO TFT could achieve the maximum mobility of 30.70 $cm^2\ V^{-1}\ s^{-1}$. The GITZO TFT annealed at 400 °C performed very depletion mode

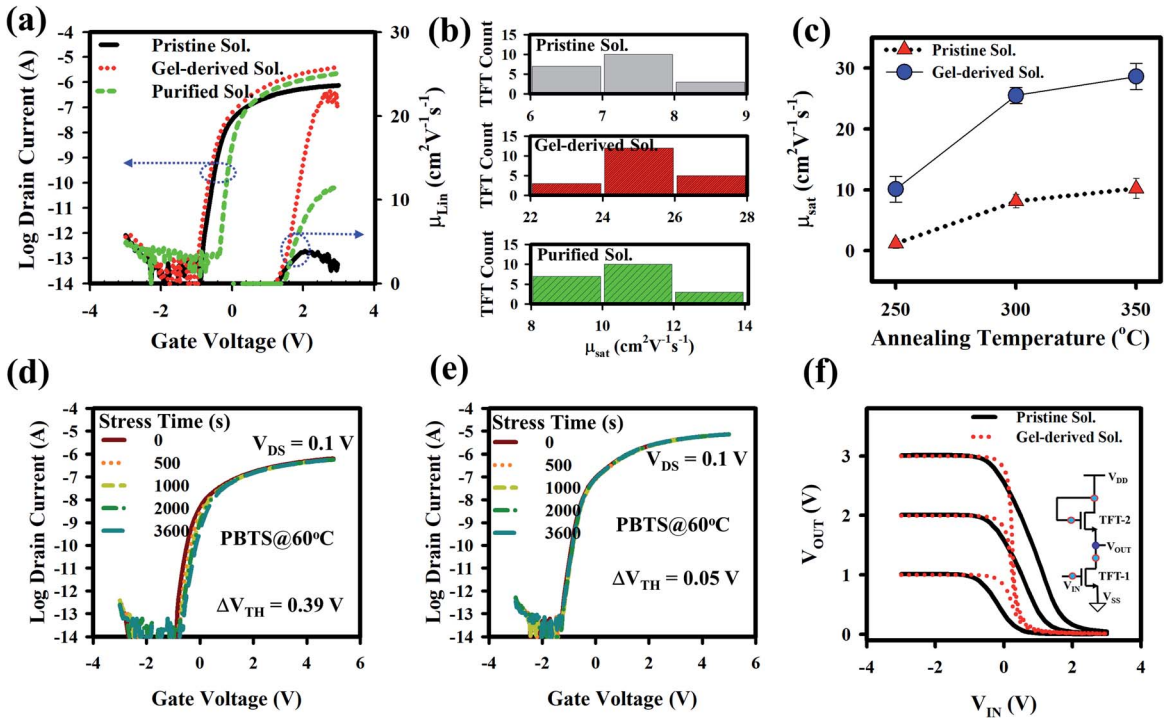

Fig. 3 Electrical properties of a-GIZTO TFT and inverter. Comparison of the (a) transfer curve and linear mobility as a function of gate voltage for pristine, gel-derived GITZO and purified GIZTO TFTs. The transfer curve of the TFTs was measured by sweeping V_{GS} from −3 to +3 V at a V_{DS} of 0.1 V. (b) Statistical analysis for the saturation mobility of 25 for pristine, gel-derived GITZO and purified GIZTO TFTs. (c) Statistical analysis for the saturation mobility of pristine and gel-derived GITZO TFTs with respect to the annealing temperature. Evolution of the transfer curve of the (d) pristine and (e) gel-derived GITZO purified GIZTO TFTs under PBTS for 1 h at 60 °C in the dark. The TFT transfer curve measured by sweeping V_{GS} from −3 to +5 V at a V_{DS} of 0.1 V. The TFTs had *W*/*L* of 20 μm/10 μm. (f) The comparison of the voltage transfers characteristic (VTC) of the pristine and gel-derived GITZO inverter at a V_{DD} of 3 V. The inset shows a typical inverter's schematic representation.

and inferior switching characteristics (such as a large SS and I_{ON}/I_{OFF}), as shown in Fig. S7d.† The output currents (at a V_{GS} = 3 V) of the pristine and gel-derived a-GITZO TFT, respectively, at different annealing temperatures (250, 300, and 350 °C) are shown in Fig. S8a–f (ESI†). The corresponding drain currents in the saturation region are (3.22, 20.05, and 34.85) μA and (23.35, 57.34, and 70.69) μA, respectively. All TFTs show clear pinch-off and saturation behavior, and there is no current crowding in low V_{DS}, which reveals good ohmic contact between the channel layer and S/D, as shown in Fig. S8 (ESI†). The I_{DS} in the saturation region is higher for the gel-derived a-GITZO.[6,12]

To test the electrical stability, the positive bias temperature stress (PBTS) was performed with a V_{GS} of 5 V at 60 °C for 1 h. Fig. 3d and e show the evaluation of the transfer curves under PBTS for pristine and gel-derived a-GITZO TFTs, and their equivalent threshold voltage shift (ΔV_{TH}) values are 0.39 and 0.15 V, respectively. This slight shift in the ΔV_{TH} is due to less trap density at the semiconductor/GI interface. The time constant (τ) and stretched exponential exponent (β) extracted from the stretched-exponential equation ($\Delta V_{TH} = \Delta V_0\{1 - \exp[-(t/\tau)^{\beta}]\}$, where ΔV_0 is ΔV_{TH} at an infinite time), are shown in Fig. S9a and b (ESI†). The τ and β values are 2.48×10^5 s and 1.07×10^6 s, and 0.65 and 0.53 for the TFTs using the pristine and gel-derived GITZO, respectively. Therefore, the longer τ value of the gel-derived GITZO TFT is due to fewer interface traps.[6,10,11,44] Fig. 3f shows the comparison of the voltage transfer characteristic (VTC) of the pristine and gel-derived GITZO inverters. The VTC was measured by sweeping a supplied voltage (V_{DD}) from 0 to 3 V (step = 1 V) with a V_{SS} of 0 V. The GITZO inverter exhibits the maximum gain ($-\partial V_{OUT}/\partial V_{IN}$) of 12.16 V/V (gel-derived), whereas 1.65 V/V (pristine) at 3 V, as shown in Fig. S9c (ESI†). Comparison of the transfer and output curves of spray-pyrolyzed ZnO TFT with pristine and gel-derived precursor solutions are shown in Fig. S10a (ESI†). The gel-derived ZnO TFT exhibits superior electrical properties compared to the pristine one. The mobility increased from 11.18 to 24.83 $cm^2 V^{-1} s^{-1}$, and V_{ON} shifts towards a positive direction from −1.93 to 0.90 V. The comparison of mobility, V_{TH}, and SS for the pristine and gel-derived spray-pyrolyzed ZnO TFTs are shown in Fig. S10b (ESI†). Both output curves of the ZnO TFTs show clear pinch-off and saturation behavior and no current crowding in low V_{DS}, which reveals good ohmic contact between the semiconductor and S/D region (see Fig. S10c, ESI†).

The extinction coefficient (epsilon2) spectra for the pristine, gel-derived, and purified GITZO precursor solution-based film were measured by spectroscopy ellipsometry (SE), as shown in Fig. 4a. The change in band-edge states for all three samples was analyzed by the deconvolution of the epsilon2 spectra into two separate band-edge states: deep band-edge state (D1) and shallow band-edge state (D2) below the conduction band.[9,15,19] The area ratio of D1 for pristine, gel-based, and purified GITZO are 28.34, 17.39, and 22.37%, respectively, and 71.66, 82.61, and 77.63% for D2. The D1 ratio significantly reduces from 28.34 to 17.39%, consequently increasing the density of the D2 ratio from 71.66 to 82.61% by gel-derived GITZO precursor. The reduction of the D1 ratio leads to hysteresis-free TFT, whereas the higher area of D2 could easily donate the electron and enhance mobility. Slight VTH shifts in the negative direction and higher ON current of the gel-derived GITZO TFT are due to the energy level of D2 being close to the conduction band compared to the pristine one.[9,19] According to the percolation conduction, the shallow donor states can contribute to the increase of mobility.[9,15,19] Less D1 states are responsible for electron-trap states during PBTS, leading to the negligible ΔV_{TH} shift in GITZO TFT by the gel-derived precursor solution.[19] Fig. 4b shows the histogram to compare the band-edge states of the pristine, gel-derived, and purified GITZO precursor solution-based film. The reduction of defect states in the gel-derived precursors is further confirmed by XPS (chemical bonding analysis of the O 1s peak). Fig. 4c and d shows the XPS spectra for the O 1s peaks of the pristine and gel-derived GITZO films deposited on the ZrO_x layer, respectively. The XPS peaks for the O 1s core level are deconvoluted into three sub-peaks centered at the binding energy of 529.26 eV (M–O, metal–oxygen), 530.20 eV (V_o, oxygen vacancies), and 531.10 eV (–OH, hydroxyl group). From the XPS analysis, the M–O bonding ratio increases from 65.08 to 75.86%, while the V_o ratio decreases from 23.01 to 17.32%, and the –OH ratio decreases from 11.91 to 6.82% by using gel-derived GITZO.[7,13] The defect states analysis from the epsilon2 spectra and chemical bonding analysis from deconvoluted O 1s spectra for the gel-derived GITZO confirm fewer defects and a higher M–O bonding ratio. The higher M–O–M network leads to an increase in the metal s orbital overlap.[26,42] The increase in the overlap leads to higher mobility. Fig. 4e shows the M–O–M network and defects (V_o + –OH) with respect to the depth of the film, where the deconvolution of O 1s peak occurs at a different (0, ∼3, ∼6, and ∼9 nm) depths from the GITZO surface. It is clear that the bulk of the GITZO film consists of higher M–O bonds and less defect states. The improvement of the film quality can be further confirmed from XRR analysis. Fig. 4f shows the histogram for film densities showing 5.23 and 6.02 g cm^{-3}. It should be noted that the refractive index and surface roughness values are consistent with film density using XRR analysis. Fig. 4g illustrates the charge transport model for the GITZO thin films using pristine and gel-derived precursor solutions. The increase of the film density indicates a better film quality with a proper conduction path for electron transportation, and thus improves the switching properties of the TFT.

The GIZTO TFT was also fabricated on polyimide (PI)/carrier glass, followed by detaching the glass with a non-laser method.[20,21,46] The transfer curves of the a-GIZTO TFT were measured with the TFTs bent on a cylinder of 3 mm radius, as shown in Fig. S11a.† There is no V_{DS} dependency of the TFT when measured with a V_{DS} of 0.1 and 1.1 V. The μ_{FE} is 11.89 $cm^2 V^{-1} s^{-1}$, V_{ON} is −0.54 V, and SS 144 mV dec^{-1}. The transfer curve with zero hysteresis voltage with a bending radius of 3 mm can be seen in Fig. S11b.† The output curves of a-GITZO TFT show a clear pinch-off and saturation behavior, as shown in Fig. S11c (ESI†). There is no current crowding at a low V_{DS}, which reveals the excellent ohmic contact between the semiconductors and S/D contacts.[21] Fig. 5a shows the transfer curve after out-folding cycles until 50k. The inset of Fig. 5a shows the experimental setup for the out-folding test with a radius of 3 mm. Fig. 5b shows the ΔV_{TH} as

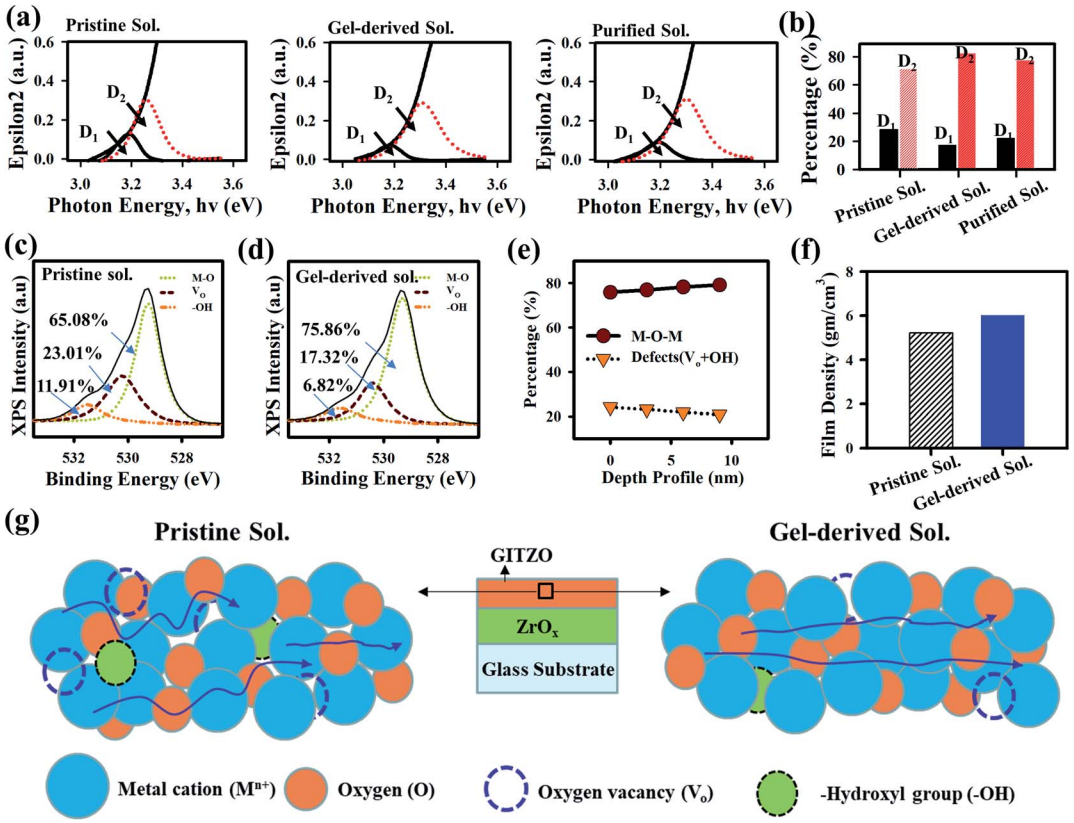

Fig. 4 Defect states and chemical bonding analysis of the GITZO thin film. (a) Extinction coefficient (epsilon2) spectra as a function of photon energy, and (b) the histogram for comparison of the deep band-edge state (D1) and shallow band-edge state (D2) below the conduction band. XPS spectral analysis of the deconvoluted O 1s peak intensity for (c) the pristine and (d) gel-derived GITZO films. The individual contributions of the metal oxide (M–O), oxygen vacancy (V_o), and a metal hydroxyl group (M–OH) are centered at (~529.5 eV), (~532.0 eV), and (~531.0 eV), respectively. The V_o and –OH decrease significantly by gel-derived GITZO precursor solution. (e) M–O–M and defects (V_o + OH) with respect to the film depth for gel-derived GITZO films. (f) Film density of the pristine, gel-derived, and purified solution-based GITZO films. (g) Charge transportation model for the GITZO thin film with pristine and gel-derived precursor solution.

a function of bending cycles. An almost negligible V_{TH} shift of the GITZO TFT can be seen after 50k bending.

The gel-based precursor technique was applied to the p-channel CTSGO film for its TFT. The transfer characteristics for the pristine and gel-derived p-channel CTSGO TFTs are shown in Fig. 5c and d, respectively, and measured at drain voltage (V_{DS}) = −1 V by sweeping gate voltage (V_{GS}) from +2 to −5 V. It should be noted that the maximum μ_{FE} of the gel-derived CTSGO TFT is 4.25 $cm^2\ V^{-1}\ s^{-1}$. The inset of Fig. 5c and d shows the histogram for the μ_{FE} of the pristine and gel-derived CTSGO p-channel TFTs, respectively. The μ_{FE} of CTSGO TFT increases from 1.72 ± 0.28 to 3.97 ± 0.52 $cm^2\ V^{-1}\ s^{-1}$ by gel-derived precursor solution. In a p-type MO semiconductor, anisotropic, highly localized O 2p orbitals form the carrier conduction path in the valence band maximum (VBM). These lead to a large hole effective mass and inferior hole mobility (μ_h) of the p-type metal oxide semiconductor. The improvement of the electrical properties is due to the reduction of interfacial defects from 4.41 × 10^{12} to 3.54 × 10^{12} cm^{-3}, which were confirmed by calculating the interfacial traps (N_{ss}, $N_{ss} = \{SS(\log(e))/(kT/q) - 1\}(C_{ox}/q)$, where k is the Boltzmann constant (8.617 × 10^{-5} eV K^{-1}), q = 1.602 × 10^{-19} C, (kT/q = 0.0259 eV), T is the absolute temperature (300 K), and C_{ox} is the dielectric capacitance). To check the performance uniformity of the solution-processed p-channel CTSGO TFTs, we measured 12 TFTs each. Uniformity of the gel-derived p-channel CTSGO TFTs and SS values are shown in Fig. S12a and b (ESI†). The output curves of the pristine and gel-derived CTSGO TFTs are shown in Fig. S12c and d (ESI†), respectively. The output curves were measured at V_{DS} from 0 to −5 V by sweeping V_{GS} from 0 to −5 V with a step of −1.0 V. Output curves of the pristine and gel-derived CTSGO TFTs show clear pinch-off and saturation regions, where the increment of I_{DS} with increasing $-V_{GS}$ indicated the p-channel behavior.[50–53] There is no current crowding in low V_{DS}, indicating good ohmic contact between the S/D and channel layer, as shown in Fig. S12c and d (ESI†).[54–56] The turn-on voltage (V_{ON}) is defined as the gate-source voltage (V_{GS}) at which the I_{DS} rapidly increases. The electrical properties (such as mobility, V_{TH}, N_{SS}, and drain current) of CTSGO TFT are summarized in Table S2.†

The XRR spectra of the CTSGO thin films with pristine and gel-derived precursor solutions are shown in Fig. 5e, and their corresponding film densities were 3.70 and 4.10 g cm^{-3}, respectively, as shown in Fig. 5f. The oscillations in the XRR

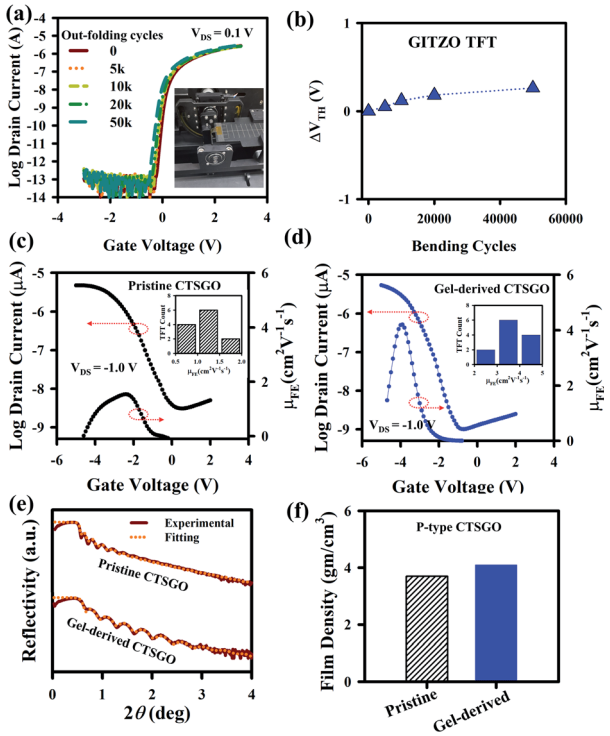

Fig. 5 Electrical properties of the low-temperature processed n-channel flexible GITZO and p-channel CTSGO TFT annealed at 250 °C. (a) Evaluation of the GIZTO TFT transfer curves under tensile stress bending with a radius of 3 mm for 50k bending cycles. Inset of (a) shows the photograph of the flexible gel-derived GITZO TFT measurement when it is flat and bending with a 5 mm. (b) ΔV_{TH} as a function of stress time. The TFTs had a W/L of 20 μm/10 μm. The transfer curve and linear mobility as a function of the gate voltage for (c) pristine and (d) gel-derived CTSGO TFT. Inset of (c) and (d) shows the histogram for the mobility of 12 pristine and gel-derived CTSGO TFTs, respectively. Comparison for the (e) X-ray reflectivity (XRR) spectra and (f) histogram of the CTSGO film density with pristine and gel-derived precursor solution.

spectra and critical angle are related to the surface morphology and film density, respectively. The gel-derived CTSGO film exhibits higher film density, which reveals that the absorption of moisture can be reduced. The gel-derived CTSGO can achieve a good interface between the GI/channel and channel/(S/D) electrodes. These results suggest that the gel-derived precursor solution could increase the film density by reducing the defects/porosity of the film, which was further confirmed by measuring the refractive index (RI) using ellipsometry spectroscopy. The RI value for gel-derived (2.27) is higher than pristine (2.10), as shown in Fig. S12e (ESI†), indicating the compactness of the film increased by gel-derived precursor solution (ESI†). The reduction of the porosity and increase of film density would enhance the TFT performance.[55,56,59] The thin-film properties, such as film density, RI, surface energy, and work adhesion, for the CTSGO are summarized in Table S3 (ESI†). Therefore, a gel-derived metal–oxide precursor solution could improve the thin-film quality. The electrical properties (such as mobility, SS, ΔV_{TH}) for multi-component metal–oxide based TFTs are summarized in Table S4.†

Conclusion

In conclusion, we have developed the high mobility of the gel-derived GITZO thin-film transistor (TFT) using ZrO_x as the gate insulator. The gel-derived GITZO film gives an excellent interface with ZrO_x. The GITZO TFT exhibits the saturation mobility (μ_{sat}) of 28.6 ± 2.15 cm^2 V^{-1} s^{-1}, which is three-fold higher than the pristine one, and excellent stability under positive-bias-temperature stress (PBTS) with a small ΔV_{TH} of 0.15 V at a V_{GS} of 5 V for 1 h. In addition, the technique was applied to p-type CTSGO TFT, and its μ_{FE} increases from 1.71 to 4.25 cm^2 V^{-1} s^{-1} by implementing the gel-derived precursor technique. The enhancement is due to the high quality of the film, less impurity concentration, and fewer interfacial traps between the semiconductor and GI. Therefore, the gel-derived metal–oxide precursor could be used for improving the performance of both n- and p-channel TFTs for the next-generation TFT electronics.

Author contributions

All of the authors contributed equally to this work.

Conflicts of interest

We declare no conflicts related to this paper.

Acknowledgements

This work was supported by the Technology Innovation Program (or Industrial Strategic Technology Development Program (20010082, Development of low-temperature patterning and heat treatment technology for light and thermal stability in soluble oxide TFT manufacturing)) funded by the Ministry of Trade, Industry & Energy (MI, Korea).

References

1 K. Nomura, H. Ohta, A. Takagi, T. Kamiya, M. Hirano and H. Hosono, *Nature*, 2004, **432**, 488–492.
2 D. H. Lee, Y. J. Chang, G. S. Herman and C. H. Chang, *Adv. Mater.*, 2007, **19**, 843–847.
3 P. T. Tue, T. Miyasako, J. Li, H. T. C. Tu, S. Inoue, E. Tokumitsu and T. Shimoda, *IEEE Trans. Electron Devices*, 2013, **60**, 320–326.
4 R. Lu, J. Lu, X. Wei, S. Yue, S. Li, B. Lu, Y. Zhao, L. Zhu, L. Chen and Z. Ye, *Adv. Electron. Mater.*, 2020, **6**, 2000233.
5 H. Hosono, *J. Non-Cryst. Solids*, 2006, **352**, 851–858.
6 R. N. Bukke, N. N. Mude, J. K. Saha and J. Jang, *Adv. Mater. Interfaces*, 2019, **6**, 1900277–1900285.
7 S. Parthiban and J. Y. Kwon, *J. Mater. Res.*, 2014, **29**, 1585–1596.
8 J. W. Hennek, J. Smith, A. Yan, M. G. Kim, W. Zhao, V. P. Dravid, A. Facchetti and T. J. Marks, *J. Am. Chem. Soc.*, 2013, **135**, 10729–10741.
9 J. B. Ko, S. H. Lee, K. W. Park and S. K. Park, *RSC Adv.*, 2019, **9**, 36293–36300.

10 N. N. Mude, R. N. Bukke, J. K. Saha, C. Avis and J. Jang, *Adv. Electron. Mater.*, 2019, **5**, 1900786.
11 I. M. Choi, M. J. Kim, N. On, A. Song, K. B. Chung, H. Jeong, J. K. Park and J. K. Jeong, *IEEE Trans. Electron Devices*, 2020, **67**, 1014–1020.
12 M. Ochi, *SID Int.–Symp. Dig. Tech. Pap.*, 2015, **46**, 853–856.
13 X. H. Lu, *SID Int.–Symp. Dig. Tech. Pap.*, 2017, **48**, 291–293.
14 T. Amorphous, *SID Int.–Symp. Dig. Tech. Pap.*, 2015, **46**, 766–768.
15 Y. S. Kim, H. M. Lee, J. H. Lim and J. S. Park, *Appl. Phys. Lett.*, 2020, **117**, 143505.
16 D. Liu, L. Jia, J. Su, Y. Ma, R. Li, S. Dai, Y. Wang, H. Yang and X. Zhang, *J. Mater. Sci.: Mater. Electron.*, 2019, **30**, 7016.
17 J. W. Jo, K. H. Kim, J. Kim, S. G. Ban, Y. H. Kim and S. K. Park, *ACS Appl. Mater. Interfaces*, 2018, **10**, 2679–2687.
18 G. Adamopoulos, S. Thomas, P. H. Wöbkenberg, D. D. C. Bradley, M. A. McLachlan and T. D. Anthopoulos, *Adv. Mater.*, 2011, **23**, 1894–1898.
19 J. Sheng, H. J. Lee, S. Oh and J. S. Park, *ACS Appl. Mater. Interfaces*, 2016, **8**, 33821–33828.
20 M. Mativenga, D. Geng, B. Kim and J. Jang, *ACS Appl. Mater. Interfaces*, 2015, **7**, 1578–1585.
21 R. N. Bukke, J. K. Saha, N. N. Mude, Y. G. Kim, S. Lee and J. Jang, *ACS Appl. Mater. Interfaces*, 2020, **31**, 35164–35174.
22 R. A. John, N. A. Chien, S. Shukla, N. Tiwari, C. Shi, N. G. Ing and N. Mathews, *Chem. Mater.*, 2016, **28**, 8305–8313.
23 R. N. Bukke, C. Avis and J. Jang, *IEEE Electron Device Lett.*, 2016, **37**, 433–436.
24 B. R. Naik, C. Avis, M. D. H. Chowdhury, T. Kim, T. Lin and J. Jang, *Jpn. J. Appl. Phys.*, 2016, **55**, 03CC02.
25 A. Liu, Z. Guo, G. Liu, C. Zhu, H. Zhu, B. Shin, E. Fortunato, R. Martins and F. K. Shan, *Adv. Electron. Mater.*, 2017, **3**, 1600513–1600523.
26 R. N. Bukke, M. N. Naik, C. Avis and J. Jang, *IEEE Electron Device Lett.*, 2018, **39**, 371–374.
27 Y. Chen, B. Wang, W. Huang, X. Zhang, G. Wang, M. J. Leonardi, Y. Huang, Z. Lu, T. J. Marks and A. Facchetti, *Chem. Mater.*, 2018, **30**, 3323–3329.
28 H. J. Chen, Y. S. Rim, C. Y. Jiang and Y. Yang, *Chem. Mater.*, 2015, **27**, 4713–4718.
29 K. K. Banger, R. L. Peterson, K. Mori, Y. Yamashita, T. Leedham and H. Sirringhaus, *Chem. Mater.*, 2014, **26**, 1195–1203.
30 K. H. Lee, J. H. Park, Y. B. Yoo, W. S. Jang, J. Y. Oh, S. S. Chae, K. J. Moon, J. M. Myoung and H. K. Baik, *ACS Appl. Mater. Interfaces*, 2013, **5**, 2585–2592.
31 P. T. Erslev, E. S. Sundholm, R. E. Presley, D. Hong, J. F. Wager and J. D. Cohen, *Appl. Phys. Lett.*, 2009, **95**, 192115–192120.
32 K. Jiang, S. T. Meyers, M. D. Anderson, D. C. Johnson and D. A. Keszler, *Chem. Mater.*, 2013, **25**, 210–214.
33 H. Yang, J. Su, R. Li, L. Jia, D. Liu, Y. Ma and X. Zhang, *Superlattices Microstruct.*, 2020, **141**, 106489–106493.
34 J. W. Park, B. H. Kang and H. J. Kim, *Adv. Funct. Mater.*, 2019, **21**, 1904632–1904671.
35 K. Jiang, J. T. Anderson, K. Hoshino, D. Li, J. F. Wager and D. A. Keszler, *Chem. Mater.*, 2011, **23**, 945–952.
36 K. K. Banger, Y. Yamashita, K. Mori, R. L. Peterson, T. Leedham, J. Rickard and H. Sirringhaus, *Nat. Mater.*, 2011, **10**, 45–50.
37 J. Chung, Y. J. Tak, W. G. Kim, J. W. Park, T. S. Kim, J. H. Lim and H. J. Kim, *J. Mater. Chem. C*, 2018, **6**, 4928–4935.
38 X. Yu, J. Smith, N. Zhou, L. Zeng, P. Guo, Y. Xia, A. Alvarez, S. Aghion, H. Lin, J. Yu, R. P. Chang, M. J. Bedzyk, R. Ferragut, T. J. Marks and A. Facchetti, *Proc. Natl. Acad. Sci. U. S. A.*, 2015, **112**, 3217–3222.
39 L. Lu and M. Wong, *IEEE Trans. Electron Devices*, 2015, **62**, 574–579.
40 J. K. Saha, M. M. Billah, R. N. Bukke, Y. G. Kim, N. N. Mude, A. B. Siddik, M. M. Islam, Y. Do, M. Choi and J. Jang, *IEEE Trans. Electron Devices*, 2020, **67**, 1021–1026.
41 S. H. Jeong, J. Y. Lee, S. S. Lee, Y. M. Choi and B. H. Ryu, *J. Phys. Chem. C*, 2011, **115**, 11773–11780.
42 R. N. Bukke, N. N. Mude, J. Lee, C. Avis and J. Jang, *IEEE Electron Device Lett.*, 2018, **40**, 32–35.
43 D. E. Kim, S. W. Cho, Y. B. Kim, K. S. Kim, D. H. Yoon, S. H. Jung, W. J. Kang and H. K. Cho, *Ceram. Int.*, 2017, **43**, 8956–8962.
44 L. Hong, W. Xu, W. Liu, S. Han, P. Cao, M. Fang, D. Zhu and Y. Lu, *Appl. Surf. Sci.*, 2020, **504**, 1444992.
45 Y. Zhao, Z. Wang, G. i. Xu, L. Cai, T. H. Han, A. Zhang, Q. Wu, R. Wang, T. Huang, P. Cheng, S. Y. Chang, D. Bao, Z. Zhao, M. Wang, Y. Huang and Y. Yang, *Adv. Funct. Mater.*, 2020, **30**, 2003285–2003290.
46 S. Lee, D. Jeong, M. Mativenga and J. Jang, *Adv. Funct. Mater.*, 2017, **27**, 1700437–1700445.
47 X. Zhang, B. Wang, W. Huang, Y. Chen, G. Wang, L. Zeng, W. Zhu, M. J. Bedzyk, W. Zhang, J. E. Medvedeva, A. Facchetti and T. J. Marks, *J. Am. Chem. Soc.*, 2018, **140**, 12501–12510.
48 S. Parthiban and J. Y. Kwon, *J. Mater. Res.*, 2014, **29**, 1585–1596.
49 H. Zhu, A. Liu, G. Liu and F. Shan, *Appl. Phys. Lett.*, 2017, **111**, 143501.
50 H. Hu, J. Zhu, M. Chen, T. Guo and F. Li, *Appl. Surf. Sci.*, 2018, **441**, 295–302.
51 Y. Qu, J. Yang, Y. Li, J. Zhang, Q. Wang, A. Song and Q. Xin, *Semicond. Sci. Technol.*, 2018, **33**, 075001.
52 S. Baig, A. D. Hendsbee, P. Kumar, S. Ahmed and Y. Li, *J. Mater. Chem. C*, 2019, **7**, 14543–14554.
53 J. Kim, H. M. Kim, S. Cho, C. Avis and J. Jang, *Adv. Funct. Mater.*, 2018, **28**, 1802941.
54 N. N. Mude, R. N. Bukke and J. Jang, *ACS Appl. Mater. Interfaces*, 2021, **13**, 20277–20287.
55 M. D. Francesco, E. Simonetti, G. Gorgi and G. B. Appetecchi, *Challenges*, 2018, **8**, 1–17.
56 N. N. Mude, R. N. Bukke and J. Jang, *J. Mater. Chem. C*, 2021, **9**, 9188–9196.
57 F. Li, R. Tao, B. Cao, L. Yang and Z. Wang, *Adv. Funct. Mater.*, 2021, **36**, 2104367.
58 Z. Wang, X. Xiong, J. Li and M. Dong, *Mater. Today Phys.*, 2021, **16**, 100290.
59 R. N. Bukke, N. N. Mude, M. M. Islam and J. Jang, *Appl. Surf. Sci.*, 2021, **568**, 150947.